PHYSICAL REVIEW B **77**, 235423 (2008)

Effects of shadowing and steering in oblique-incidence metal (100) epitaxial growth

Yunsic Shim,* Valery Borovikov,† and Jacques G. Amar‡
Department of Physics & Astronomy, University of Toledo, Toledo, Ohio 43606, USA

(Received 4 October 2007; revised manuscript received 25 February 2008; published 16 June 2008)

The effects of attraction in oblique-incidence metal (100) epitaxial growth are studied by comparing the results of simulations which include the effects of short-range (SR) and long-range (LR) attraction with results obtained in the absence of attraction. In general, we find that the qualitative dependence of the surface morphology on deposition angle and film thickness, including the existence of a transition from mounds to asymmetric ripples oriented perpendicular to the beam at large deposition angles, as well as a second transition from ripples to rods with (111) facets oriented parallel to the beam at larger deposition angles and film thicknesses, is not altered by the presence of attraction. However, we find that attraction can have two important effects. The first effect, which is a result of steering due to LR attraction and leads to decreased shadowing, leads to decreased anisotropy in the submonolayer regime and can also lead to decreased surface roughness for high-deposition angles and intermediate film thicknesses. The second effect, due to flux focusing, leads to an increase in the surface roughness and feature size and also reduces the critical thickness for ripple and rod formations. This effect also tends to limit the anisotropy in the rod phase for high-deposition angles and film thicknesses. Surprisingly, we also find excellent scaling for the surface roughness as a function of deposition angle and film thickness in the presence of attraction. We also present extensive results for the dependence of the surface morphology on a variety of other parameters including azimuthal angle, growth temperature, deposition flux, and crystal geometry. A comparison between our simulation results and recent experimental results for grazing incidence Cu/Cu(100) growth is also presented.

DOI: 10.1103/PhysRevB.77.235423 PACS number(s): 81.15.Aa, 68.55.−a, 81.10.Aj

I. INTRODUCTION

Recently there has been a great deal of interest in understanding the detailed mechanisms controlling the surface morphology in epitaxial growth.[1,2] While much of the theoretical effort has focused on understanding the effects of various surface relaxation processes, such as the Ehrlich–Schwoebel barrier to interlayer diffusion[3] and edge and corner diffusions,[4–6] recently, attention has also focused on the deposition process. For example, in recent glancing angle deposition experiments on Cu/Cu(100) growth by van Dijken *et al.*,[7,8] which were carried out at constant deposition rate, a dramatic dependence of the surface morphology on deposition angle was observed. In these experiments a series of transitions was observed from symmetric mound structures for deposition angles up to $\theta=55°$ (where θ is the angle between the beam and the substrate normal), to asymmetric mounds with increasing slopes for deposition angles up to 70°, to asymmetric ripples oriented perpendicular to the beam with (113)/(111) facets on the shadow/illuminated sides at $\theta=80°$, and finally to symmetric pyramidal structures with (111) facets at $\theta=85°$. In addition, it was found that grazing incidence Co/Cu(001) growth[9] and Co/SiGe templates on Si(100) growth[10] generate a strong uniaxial magnetic anisotropy due to the surface anisotropy produced by oblique deposition.

Motivated in part by these experiments, as well as by earlier experiments on Cu/Cu(100) growth of Ernst *et al.*,[11] recent theoretical studies[12–14] have shown that even in the case of normal-incidence deposition, the effects of steering due to the short-range (SR) attraction of depositing atoms to step edges can significantly enhance the surface roughness. In addition, recent multiscale simulations of the early stages of Cu/Cu(100) and Cu(100) vicinal growth[15,16] have demonstrated that at large deposition angles, the long-range (LR) van der Waals attraction of depositing atoms to the surface can also play an important role. However, because of the extremely time-consuming nature of these simulations, only very recently has it become possible to extend these simulations to multilayer growth.[17,18]

Recently, we have used a simplified model with ballistic deposition[19] in order to show that many of the qualitative and semiquantitative features observed in high-angle oblique-incidence Cu/Cu(100) growth by van Dijken *et al.*[7,8] can be explained by geometrical (shadowing) effects. Our results also indicated that the formation of (111) facets is crucial to the formation of ripple structures at large angles of incidence. A second transition from ripples to rods oriented parallel to the beam was also observed at high incident angles and large film thickness. In addition, excellent scaling was obtained for the surface roughness and perpendicular correlation length as functions of film thickness and deposition angle.

However, these results do not take into account the effects of SR and LR attraction, and it is of interest to determine to what extent these effects might alter the surface morphology, as well as the picture previously presented in Ref. 19. Accordingly, here we present the results of extensive simulations of a model of metal (100) growth which is similar to that studied in Ref. 19, but in which the additional modifying effects of SR and LR attraction have been included. Our results indicate that the qualitative picture presented in earlier ballistic deposition simulations,[19] including the existence of a transition from mounds to asymmetric ripples oriented perpendicular to the beam at large deposition angles, as well as a second transition to rods with (111) facets oriented parallel to the beam at larger deposition angles and film thicknesses, is not fundamentally altered by the inclusion of SR and LR attraction. However, the results presented here also demonstrate that attraction can have several important effects. The first effect, due primarily to LR attraction, is a reduction in shadowing in the submonolayer regime which leads to decreased anisotropy in this regime. The second effect which occurs primarily in the multilayer regime is "flux focusing" due to SR and LR attraction.[7,8] This effect tends to increase the surface roughness and feature size and reduce the critical thickness for ripple and rod formations, and can also enhance the anisotropy in the early stages of multilayer growth. In the later stages of growth it also leads to "sideways attraction" which tends to limit the anisotropy in the "rod" phase. Along with the existence of a competition between ripples and rods at high-deposition angles, this second effect may explain the experimental observation of symmetric pyramids for deposition angles beyond the critical angle for ripple formation.

In addition to these results for the surface morphology in the presence of attraction, we also find excellent scaling for the surface roughness and correlation length as functions of deposition angle and film thickness.[20] A number of additional results for the dependence on other deposition parameters are also presented. These include results for the dependence of the surface morphology on growth temperature, azimuthal angle, deposition flux, and crystal geometry.

The organization of this paper is as follows. In Sec. II, we describe the model used in our simulations along with a summary of the simulation parameters and measured quantities. We then present our results in Sec. III. In particular, we first present results for the effects of SR and LR attraction on shadowing and steering followed by more detailed results for the effects of attraction on the surface morphology. Additional results for the dependence of the surface morphology on a variety of deposition parameters are also presented. Finally, in Sec. IV, we summarize and discuss our results.

II. SIMULATION DETAILS

In order to take into account the effects of shadowing as well as the attraction of depositing atoms to the substrate, we have carried out simulations using a hybrid model which combines a one-atom molecular-dynamics (MD) simulation to describe the deposition process, with kinetic Monte-Carlo (KMC) simulations to describe surface relaxation. We first describe the KMC model used in our simulations, and then describe the deposition process in more detail.

A. Kinetic Monte-Carlo model

In order to compare with previous results without attraction,[19] we have used the same KMC model as was previously used in Ref. 19 for the case of ballistic deposition. We note that this model is similar to previous models[21,22] used to study metal (100) growth at normal incidence in which the crystal geometry has been taken into account. In particular, atoms are deposited with a (per site) deposition rate F, while adatoms (monomers) on a flat terrace are assumed to diffuse with hopping rate $D=D_0e^{-E_a/k_BT}$, where E_a is the activation energy for monomer diffusion and k_B is Boltzmann's constant. Compact islands are also assumed and accordingly a moderate amount of edge and corner diffusion ($D_e=D_c=e^{-E_e/k_BT}D$) was included in our simulations, while the attachment of atoms to existing islands was assumed to be irreversible, as is reasonable for metal (100) growth at and below room temperature. Since the Ehrlich–Schwoebel (ES) barrier typically plays an important role in metal epitaxial growth, the rate for an adatom at a descending step edge to diffuse over the step is given by $D_{\mathrm{ES}}=De^{-E_{\mathrm{ES}}/k_BT}$, where E_{ES} is the Ehrlich–Schwoebel barrier.

While some simulations have been carried out using a bcc(100) geometry (see Sec. III E) in most of our simulations an fcc(100) geometry was assumed, while a deposition rate corresponding to $D/F\simeq 10^5$ was used. We note that this value of D/F is in good agreement with that expected for the experiments of van Dijken *et al.*[7,8] on oblique-incidence Cu/Cu(100) growth with deposition rate $F\simeq 0.0042$ ML/s and $T\simeq 240$ K. Therefore, it is perhaps not surprising that in our previous ballistic deposition simulations using this model,[19] excellent qualitative and even semiquantitative agreement with Cu/Cu(100) growth was already obtained. In addition, we note that while our main goal is to obtain a general understanding of the effects of attraction and of a variety of deposition parameters such as deposition angle, azimuthal angle, and deposition flux on the surface morphology, the values of the deposition rate ($F=0.0257$ ML/s), prefactor ($D_0=1.8\times 10^{11}$ s^{-1}), and activation barriers used in our simulations ($E_a=0.45$ eV, $E_e=0.125$ eV, and $E_{ES}=0.07$ eV) are identical to those previously used[21] to simulate island nucleation and mound formation in room-temperature Fe/Fe(100) growth at normal incidence.[23,24] Therefore, we expect that our simulation results may also be relevant to the room-temperature oblique-incidence growth of Fe/Fe(100). However, we have also carried out additional ballistic deposition simulations with deposition rates corresponding to values of D/F ranging from $D/F=5\times 10^3$ to 10^7 in order to understand the dependence on deposition flux, see Sec. III D. In addition, we have carried out simulations with $D/F\simeq 0$, in which all activated processes except downward funneling were assumed to be "frozen" (see Sec. II B) in order to understand the low-temperature/high-deposition rate limit.

In order to examine the dependence of the surface morphology on deposition conditions we have calculated a variety of different quantities as a function of average film thickness t in units of monolayer (ML) and deposition angle θ. These include the rms surface height or "width" w, the lateral correlation lengths $\xi_{\parallel}$ and $\xi_{\perp}$ determined from the zero crossing of the height-height correlation functions parallel and perpendicular to the beam, respectively, and the anisotropy $\alpha'=\xi_{\perp}/\xi_{\parallel}$. In order to obtain a quantitative measure of the amount of (111) facet formation at the front, back, and sides of a mound, we have also calculated the average density of local front, back, and side (111) microfacets based on the relative height of a lattice site and its in-plane nearest-neighbor (nn) sites in the four equivalent in-plane (010) directions, i.e., the (010), (001), $(0\bar{1}0)$, and $(00\bar{1})$ directions. In particular, the density of front (back) (111) microfacets was calculated by counting the number of lattice sites for which the height of both of the nn sites "toward" the beam was lower (higher) while the height of both of the nn sites "away" from the beam was higher (lower), and then dividing by the total number of lattice sites. Similarly, the density of (111) microfacets on the left (right) sides of the beam was calculated by counting the number of lattice sites for which the height of both of the nn sites to the "left" (right) of the beam was lower (higher) while the height of both of the nn sites to the "right" (left) of the beam was higher (lower), and then dividing by the total number of lattice sites.

To minimize finite-size effects our simulations were typically carried out using relatively large system sizes ranging from $L=512$ to $L=2048$. For the case of ballistic deposition our results were averaged over 30–100 runs. For the more time-consuming case of deposition with attraction, a more moderate system size ($L=512$) was used along with averages over 10 runs.

B. Deposition

In order to distinguish between the geometrical effects of shadowing and the effects of steering due to attraction, we have carried out simulations both with SR and LR attraction as well as without attraction (ballistic deposition). In both cases, the depositing atom is launched from a random position above the substrate and at a height equal to the height of the highest point of the film plus the cutoff distance r_{cut}, and with a selected deposition angle θ with respect to the substrate normal. In most cases the azimuthal angle ϕ was chosen such that the deposition direction was parallel to the close-packed step edge, i.e., along the [110] direction, as in the experiments of Refs. 7 and 8. However, we have also carried out some simulations with deposition along the [100] direction in order to determine the effects of azimuthal angle on the surface morphology and roughness. The initial kinetic energy of the deposited atom corresponded to the average value $\bar{K}_i=2k_BT_m$ (where T_m is the melting temperature of the depositing material). Since our goal is to determine the general effects of attraction on the surface morphology in metal (100) growth, for simplicity we have chosen deposition parameters corresponding to Cu/Cu(100) growth, i.e., $T_m=1356$ K and $\bar{K}_i\simeq 0.20$ eV.

Since a full MD simulation of each deposition event is prohibitive for the system sizes ($L=512$ and larger), film thicknesses (up to 50 ML) and number of runs (10–100 runs) considered here, in our simulations the substrate atoms were all held fixed at their lattice positions while a one-atom MD simulation of the trajectory of the depositing atom was carried out. In particular, the depositing atom undergoes a one-atom MD simulation until its distance to the closest substrate atom is equal to the nearest-neighbor distance $a_1=a/\sqrt{2}$ (where a is the crystal lattice constant). At that point, the particle is then assumed to "cascade" randomly via downward funneling[25] (DF) from a site corresponding to this atom, until it reaches a fourfold hollow site. Thus, in our model atoms deposited on (111) microfacets are assumed to diffuse essentially instantaneously via DF to the terrace below. When considering the extremely low barriers for diffusion on metal (111) surfaces [approximately 0.05 eV for Cu(111) (Ref. 26)], this is a very reasonable approximation except at extremely low temperatures. We note that the inclusion of rapid DF in our model implies that the maximum selected mound angle corresponds to a (111) facet.

In order to estimate the possible errors in our one-atom MD simulations, we have also carried out fully multiscale simulations of deposition, in which a full-scale MD simulation of the depositing atom and nearby substrate atoms is carried out for each deposition, for a few special cases. Comparison with these results indicates that our one-atom MD approach takes into account the bulk of the effects due to LR and SR attraction, and is thus a good approximation. However, it slightly underestimates the effects of the SR interaction after collision with the substrate.[14]

While a relatively efficient "restricted" four-neighbor search was used in our previous ballistic deposition simulations[19] to identify the nearest lattice site to the depositing atom at each point of the deposition process, in most of the results presented here, a more accurate "extended" nine-neighbor search was used. While there is very little difference in the qualitative behavior, the surface roughness obtained from simulations using the extended search is slightly larger than when using the restricted search. This suggests that the extended search method leads to enhanced uphill funneling (or equivalently reduced downhill funneling) near step edges, in good agreement with MD simulations,[14,27] thus resulting in a larger surface roughness. It is also interesting to note that in the case of ballistic deposition at normal incidence ($\theta=0$), the surface roughness obtained using the restricted search is in perfect agreement with the results of ordinary KMC simulations with DF in which the deposition site is selected randomly rather than via molecular dynamics.

As in several previous simulations of steering effects in Cu/Cu(100) growth,[14–16] in our simulations with attraction, we have used a Lennard–Jones (LJ) copper potential[28] of the form

$$V_{\text{LJ}}(r) = 4\epsilon\left[\left(\frac{\sigma}{r}\right)^{12} - \left(\frac{\sigma}{r}\right)^{6}\right], \tag{1}$$

(where $\epsilon=0.4093$ eV and $\sigma=2.3377$ Å) to represent the SR interaction. We note that in previous MD simulations of adatom deposition near Cu(100) close-packed steps,[14] it was found that the results obtained using this potential with a cutoff distance $r_{\text{cut}}^{\text{SR}}=2\sigma$ which is close to that of a more sophisticated embedded-atom-method (EAM) Cu potential,[29] were essentially identical to those obtained using the EAM potential.

In order to include the effects of LR interactions, we have also included a LR van der Waals attraction[7,30] for atoms which are farther than the cutoff distance for the short-range interaction. To speed up our simulations, the LR interaction was divided into two parts. The first part corresponds to the LR attraction between the depositing atom and the semi-infinite slab below the last completely filled layer of the substrate, and has the form $U_{\text{LR}}(z)=-C_3/z^3$ (where z is the height of the depositing atom above this layer). The main effect of this interaction is to bend the path of the depositing atom as it approaches the substrate. The second part corresponds to pair interactions with the atoms above the last completely filled layer of the substrate and has the form $V_{\mathrm{LR}}(r)=-C_6/r^6$, where r is the distance between the depositing atom and the substrate atom. At high angles, this interaction can lead to flux focusing toward protruding structures which can significantly enhance the surface roughness.[7]

As for the SR interaction, the values of the constants describing the long-range interaction [$C_3=2.1$ eV Å^3 and $C_6=(3a^3C_3/2\pi)\simeq 47.2$ eV Å^6, where a is the lattice constant of Cu] were chosen to correspond to Cu/Cu(100). We note that these values were obtained in a previous calculation[30] and are significantly weaker than predicted by the LR ($1/r^6$) portion of the LJ Cu potential. Therefore, to avoid a discontinuity we have used the following expression for the pair potential in our simulations:

$$V_T(r)=[1-f(r)]V_{\mathrm{LJ}}(r)+f(r)V_{LR}(r), \tag{2}$$

where $f(r)=1/[1+e^{-(r-2\sigma)/R}]$ is the sigmoid function centered on $r=2\sigma$ with width $R=0.125\sigma$. To save computation time in our calculations of the pair interaction, a long-range cutoff $r_{\mathrm{cut}}=7\sigma$ was used, since the results were found not to depend on the cutoff for larger values.

III. RESULTS

A. Effects of attraction on steering and shadowing

In order to understand the effects of SR and LR attraction on shadowing and steering during deposition, we have first compared the flux distribution for atoms deposited near a large 50×50 single-layer-high island with the corresponding results obtained using ballistic deposition. We note that similar calculations have been carried out by van Dijken *et al.*[7,8] although in this case a much stronger LR interaction [corresponding to the LR portion of the LJ Cu interaction in Eq. (1)] was used. Figure 1 shows the normalized flux distribution profile (averaged over the width of the island) for two deposition angles $\theta=55°$ and $\theta=80°$. As can be seen, for both the case of ballistic deposition and deposition with attraction, the flux near the front edge of the island ($40<x/a_1<50$) is enhanced due to shadowing and/or steering effects, which increase with deposition angle. However, in the case of ballistic deposition, this enhancement only occurs at the bottom and top of the front step edge, while in the case of attraction it is "smeared" out over a significantly larger region beyond the step. Similarly, while the size of the shadowed region beyond the back edge of the island also increases with deposition angle [see Fig. 1(b)] it is again significantly larger in the case of attraction than in the case of ballistic deposition. However, due to steering effects, in the case of attraction the amount of shadowing immediately behind the island is less than in the case of ballistic deposition. As discussed in Sec. III B, this leads to decreased submonolayer anisotropy in the case of deposition with attraction when compared to ballistic deposition.

In order to quantify the effects of steering due to LR attraction in the early stages of growth, we have calculated the impact angle $\theta_I(z)$ of atoms approaching a flat substrate as a function of the vertical distance z from the substrate for various deposition angles. Here the angle $\theta_I(z)$ is calculated using $\theta_I=\tan^{-1}(v_z/v_{\|})$, where v_z and $v_{\|}$ are the components of the velocity of the depositing atom perpendicular and parallel to the substrate. As can be seen in Fig. 2(a), due to LR attraction, there is a significant difference between the initial deposition angle θ and the impact angle near the substrate, especially for large deposition angles. It is this steering effect which reduces the effects of shadowing in the submonolayer growth regime, when compared to ballistic deposition for large deposition angles.

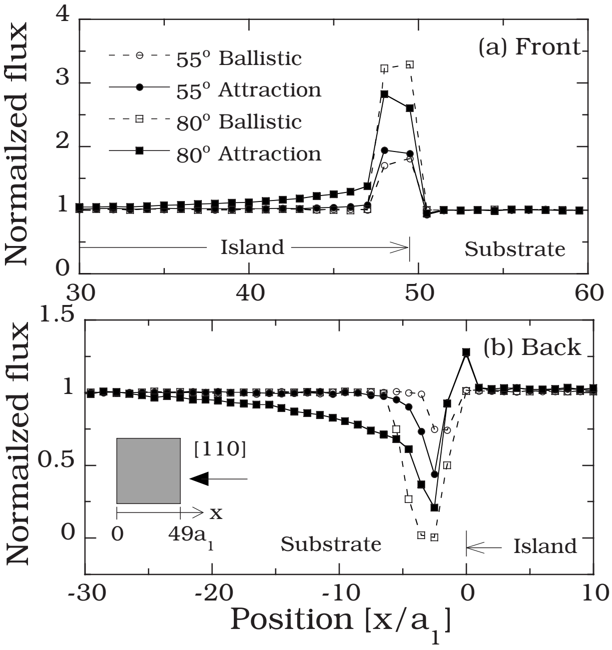

FIG. 1. Normalized deposition flux near a one-layer-high square island (corresponding to $0\leq x/a_1\leq 49$) for deposition angles $\theta=55°$ and 80° with attraction (filled symbols) and without attraction (open symbols). (a) Front side and (b) back side. Inset shows orientation of island with respect to particle beam. Error bars (not shown) are smaller than symbol size.

To quantify the effects of steering due to LR attraction in the later stages of growth, we have also measured the average "impact" angle at a distance $r=2\sigma$ from the surface, for the case of slow deposition with $D/F=10^5$ and $E_{\mathrm{ES}}=0.07$ eV, as a function of film thickness as shown in Fig. 2(b). As can be seen, with increasing film thickness the effects of steering due to LR attraction become weaker and as a result the effects of shadowing become more important. This reduction in the degree of "downward steering" due to attraction is due to the increase in the film roughness with increasing thickness, which implies that the depositing atom remains farther from most of the substrate before being "focused" on a local peak or protuberance. Thus, while steering due to attraction can substantially alter the time evolution of the surface morphology, at large film thicknesses the effects of shadowing become dominant as characteristic structures such as mounds and ripples are developed on the surface of growing films. We now consider the effects of SR and LR attraction on the surface morphology.

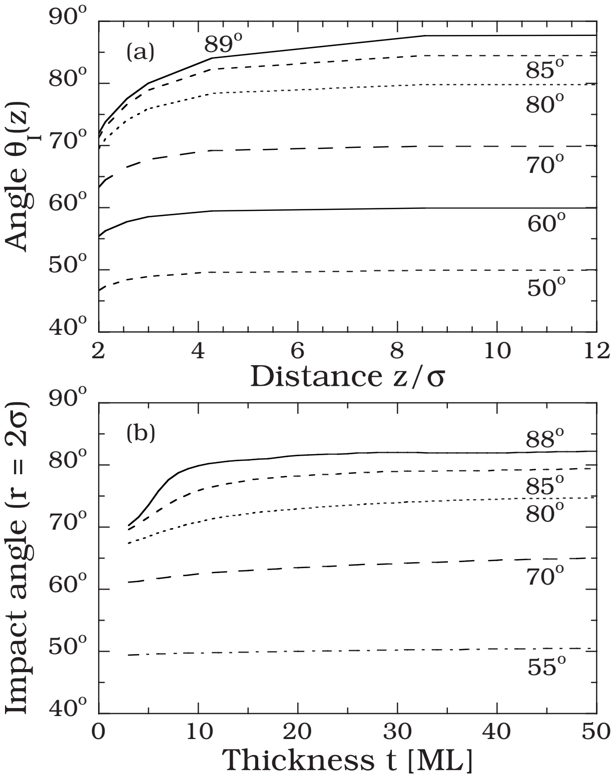

FIG. 2. (a) Incidence angle $\theta_I(z)$ of depositing atoms as a function of distance z/σ above a flat substrate in the case of LR attraction. (b) Average impact angle at a distance $r=2\sigma$ above a growing film as a function of film thickness. All results are for $D/F=10^5$ and moderate ES barrier. Error bars (not shown) are comparable to line thickness.

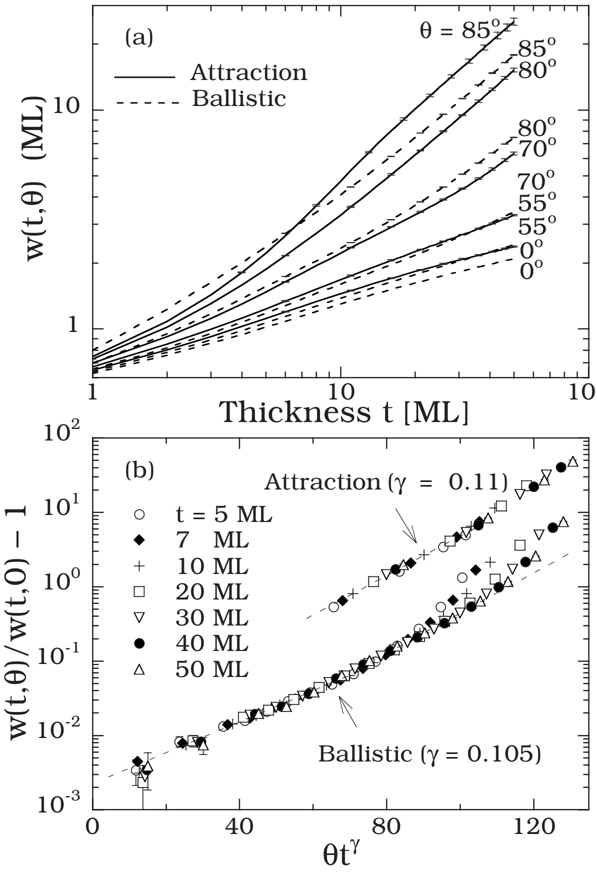

FIG. 3. (a) Surface roughness as a function of film thickness for $\theta=0°-85°$ with and without attraction (ballistic deposition). (b) Relative width deviation $\delta w/w(t,0)$ as function of scaled deposition angle θt^{γ} for $\theta=55°-85°$ (with attraction) and $\theta=10°-85°$ (without attraction) and $t=5-50$ ML for the cases given in (a). The scaling result in the case of attraction has been shifted up by a factor of 5 for clarity. All results are for $D/F=10^5$ with a moderate ES barrier.

B. Effects of attraction on surface morphology

In order to distinguish the effects of attraction from those of shadowing, we have carried out simulations both with and without attraction for the case of $D/F=10^5$ and $E_{ES}=0.07$ eV. Figure 3(a) shows the corresponding results for the surface width as a function of film thickness for deposition angles ranging from 0° to 85°. As can be seen, both with and without attraction the surface roughness and effective growth exponent β (where $w\sim t^{\beta}$) increase with deposition angle. In particular, the effective exponent β at large film thicknesses increases from a value close to 1/4 at small angles to a value close to 1 at large angles. However, in the case of attraction both the roughness and effective exponent β are larger at large film thicknesses than in the case of ballistic deposition due to the effects of flux focusing.

The behavior for large deposition angles ($\theta\geq 70°$) is particularly interesting. For example, while the "enhancement" of the surface roughness due to attraction tends to increase with deposition angle, for very large deposition angles ($\theta=85°$) the relative enhancement of the surface roughness due to attraction is actually somewhat lower than at a somewhat lower angle ($\theta=80°$). In addition, for $\theta=85°$, the roughness at small film thicknesses ($t<6$ ML) is actually lower in the case of attraction than in the case of ballistic deposition. This is due to the fact that at very high-deposition angles and small thicknesses, the effects of shadowing are significantly reduced by the LR attraction which decreases the effective deposition angle, as discussed in Sec. II A. However, at higher thicknesses, the LR steering effect is reduced [see Fig. 2(b)], since the depositing atom remains farther from the substrate before impacting the surface, as discussed in Sec IIA. As a result, the surface is again rougher in the case of attraction due to flux focusing.

Figure 3(b) shows the corresponding scaling results[31] for the relative deviation in the width $w(t,\theta)$ compared to the width at normal incidence as a function of the scaling variable θt^{γ}. As can be seen, there is excellent scaling both with and without attraction over a large range of deposition angles and film thicknesses, although there are some small deviations for the case of ballistic deposition with angles larger than 80°. Interestingly, the scaling exponent $\gamma\simeq 0.11$ is approximately the same in both cases, although somewhat larger than the value ($\gamma\simeq 0.075$) previously obtained in ballistic deposition simulations with restricted search.[19] In addition, the approximate linear behavior of the scaling function on a semilog plot clearly indicates that the relative width deviation increases exponentially with increasing deposition angle in both cases, while the small value of the exponent γ

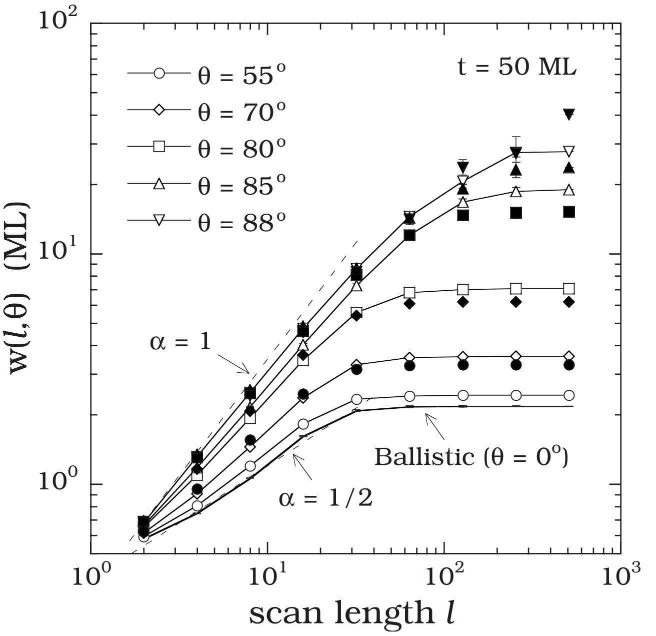

FIG. 4. Surface roughness as a function of scan length l for $\theta = 55°-88°$ for $D/F = 10^5$ with system size $L = 512$. Filled (open) symbols correspond to deposition with (without) attraction with the same type of symbol for each angle. Dotted lines are guide lines with slopes $\alpha = 1/2$ and 1.

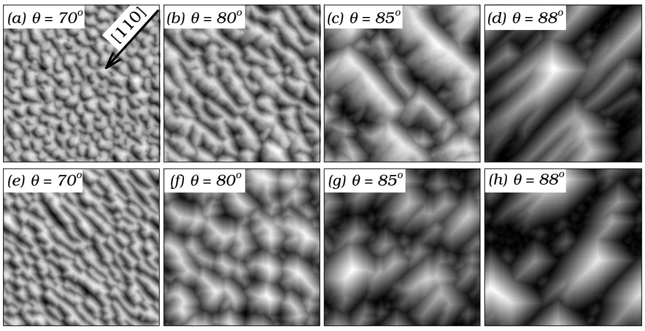

FIG. 5. Gray-scale pictures of surface morphology for $\theta = 70°-88°$ with $L = 512$ at $t = 50$ ML. Here, (a)–(d) are for ballistic deposition while (e)–(h) correspond to case of deposition with attraction. Arrow in (a) indicates deposition direction.

indicates a much weaker dependence on the film thickness t.

We have also examined the effect of oblique-incidence deposition on the surface roughness exponent α. Figure 4 shows the rms height fluctuation w_l measured over a square region of size $l \times l$ at $t = 50$ ML as a function of the scan size l. For small l, the surface width exhibits power-law behavior with $w \sim l^{\alpha}$, where α is the roughness exponent, and it saturates for large l (when the scan length l is larger than the lateral correlation length ξ). As can be seen, the effective roughness exponent increases from a value of approximately 1/2 for small deposition angles to a saturation value of 1 for large angles, although the increase with deposition angle is more rapid in the case of attraction. We note that these results imply that for small deposition angles, the value of the dynamic exponent $(z = \alpha/\beta)$ is approximately 2, but decreases with increasing deposition angle to a value close to 1.

We now examine the general effects of SR and LR attraction on the surface morphology. Figure 5 shows typical pictures of the surface at a film thickness of 50 ML for the case of ballistic deposition [Figs. 5(a)–5(d)] as well as for the case of deposition with attraction [Figs. 5(e)–5(h)] for the same set of parameters used in Figs. 3 and 4. In all cases, the resulting structures move toward the beam as they grow and coarsen. As in the simulations carried out in Ref. 19, for the case of ballistic deposition there is a series of morphological transitions with increasing deposition angle, from asymmetric mounds at $\theta = 70°$ to asymmetric ripples with (111) facets on the illuminated side at $\theta = 80°$, to larger, more well-defined ripples with some evidence of (111) side facets at $\theta = 85°$, and finally to rods with well-defined (111) front and side facets at $\theta = 88°$. On the other hand, in the case of attraction, at a thickness of 50 ML, ripples are already formed at a deposition angle $\theta = 70°$ [see Fig. 5(e)], while at $\theta = 80°$ [see Fig. 5(f)], there is an indication of competition between ripples and rods: and at $\theta = 85°$, rods are clearly visible with (111) facets. These results indicate that one of the main effects of attraction is to cause the transitions from asymmetric mounds to ripples and from ripples to rods to occur at lower thicknesses and/or mound angles than in the case of ballistic deposition. In addition, the corresponding feature sizes are larger in the case of attraction than in the case of ballistic deposition, due to flux focusing. A second important effect of attraction is to reduce the magnitude of the anisotropy in both the ripple and rod phases. For example, at $\theta = 80°$ the ripples are less pronounced and anisotropic in the case of attraction than in the case of ballistic deposition, while at $\theta = 88°$ the rods are also less anisotropic due to sideways attraction. Similarly, at $\theta = 85°$, sideways attraction tends to favor the formation of pyramidal structures [see Fig. 5(g)].

It is also interesting to compare the morphology shown in Fig. 5 with the experimental results for grazing incidence Cu/Cu(100) growth at $T = 250$ K obtained by van Dijken *et al.*[7,8] The formation of ripples with (111) facets on the illuminated sides but smaller slopes on the shadow side for deposition angle $\theta = 80°$, as shown in Fig. 5(b) for the case of ballistic deposition and Fig. 5(e) for the case of attraction, is in good qualitative and semiquantitative agreement with experiment. Similarly, our results for the case of deposition with attraction with deposition angle $\theta = 85°$ are in good qualitative agreement with the experimental observation of a pyramidal mound phase with (111) facets on all sides at this deposition angle. The onset of rotated ripples or rods at large angles $\theta = 88°$ [see Figs. 5(d) and 5(h)] and/or thicknesses is also in good agreement with very recent experimental results.[32] However, in the case of attraction, the onset of ripple formation [see Fig. 5(e)] occurs in our simulations at an angle $(\theta = 70°)$ which is somewhat lower than observed experimentally. This is most likely due to the fact that the effective rate of edge diffusion in our simulations was somewhat smaller than that expected for Cu/Cu(100) growth,[33–35] and as we have previously shown,[19] the critical angle and/or thickness for ripple formation tends to increase with increasing edge diffusion.

Our results for the surface morphology can be understood more quantitatively by measuring the anisotropy $\alpha' = \xi_{\parallel}/\xi_{\perp}$

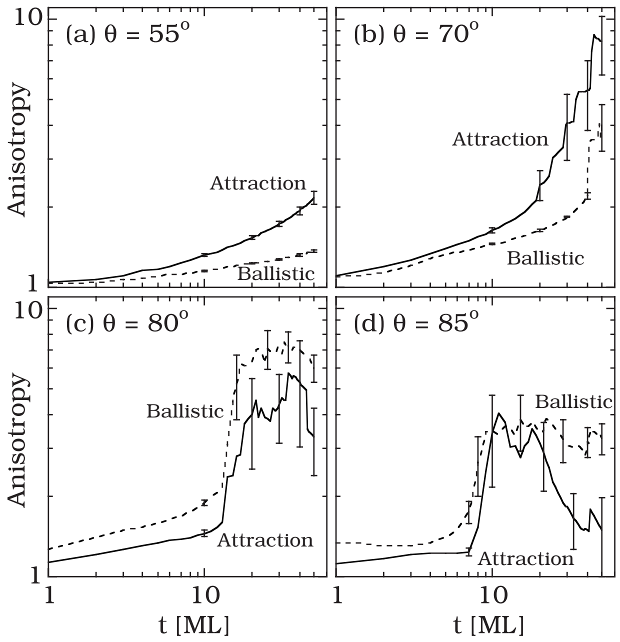

FIG. 6. Anisotropy as a function of film thickness in the case of deposition with attraction (solid lines) and without attraction (dashed) for case of $D/F=10^5$ and $E_{ES}=0.07$ eV in multilayer regime.

as a function of film thickness, as shown in Fig. 6. As can be seen, for deposition angles $\theta \geq 70°$, there is an abrupt increase in the anisotropy at a critical thickness t_c which decreases with increasing deposition angle. As indicated by the "crossing" of the *local* density of (111) facets on the "front" side and on the "shadow (back)" side which occurs at the same thickness (see Fig. 7), this abrupt increase coincides with the onset of the formation of (111) facets on the illuminated sides of mounds. Since (111) facets can efficiently capture and transport depositing atoms to the sides via DF, this leads to a strong enhancement of mound coalescence in the direction perpendicular to the beam, followed by the formation and growth of ripples with extended (111) facets on the front side. As growth continues, the (111) facets become larger while the mounds coalesce and tend to form ripples, while the anisotropy remains relatively constant. Thus, the presence of DF in our model, combined with the effects of oblique incidence provides a kinetic rather than a thermodynamic mechanism for the formation of (111) facets in oblique-incidence metal (100) growth.

For larger deposition angles and film thicknesses, the increase in anisotropy with film thickness is followed by a decrease in the anisotropy which coincides with the formation of the rod phase. As can be seen in Fig. 7(c) for $\theta = 85°$, this is accompanied by a significant increase in the density of side (111) microfacets. Figure 6 also indicates that for large angles ($\theta \geq 80°$) the anisotropy tends to be smaller in the case of attraction than in the case of ballistic deposition. However, for smaller angles ($\theta \leq 70°$) and large thicknesses, the reverse is true since the effects of steering due to LR attraction are relatively weak.

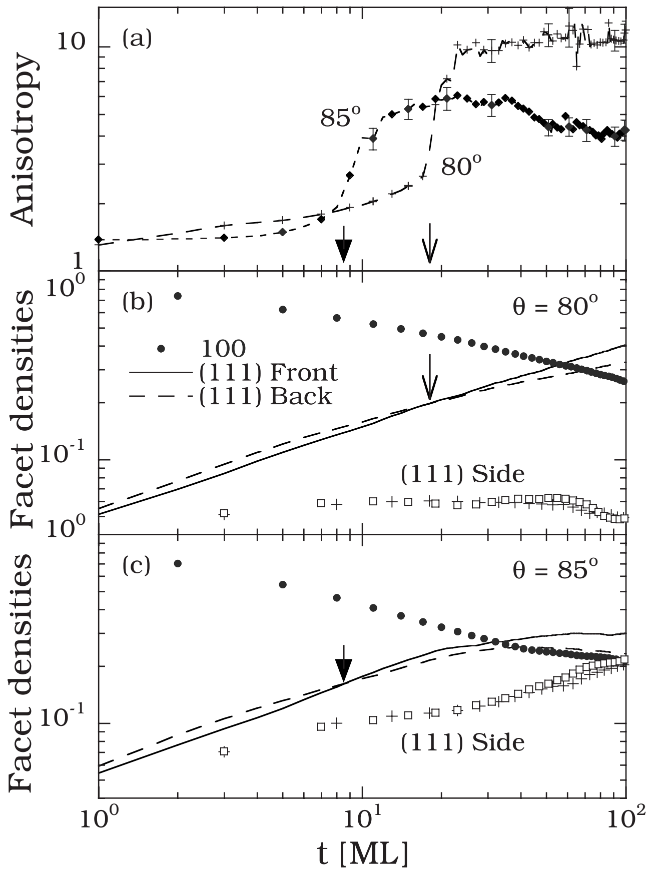

FIG. 7. (a) Anisotropy as a function of film thickness for case of ballistic deposition for $L=2048$ and $D/F=10^5$. (b) and (c) Densities of front, back, and side (111) microfacets along with (100) microfacet as a function of film thickness corresponding to (a) for $\theta = 80°$ and $\theta = 85°$.

We note that in the submonolayer regime (see Fig. 8) there is relatively little difference in the anisotropy with and without attraction for deposition angles $\theta < 80°$. However, for very large angles ($\theta \geq 80°$) the effects of steering due to LR attraction tend to reduce the effects of shadowing as already discussed, and thus significantly reduce the anisotropy. Thus, for example, for $\theta = 80°$, the calculated submonolayer anisotropy at 0.5 ML coverage in the presence of attraction is in good agreement with the value (1.05) estimated in the experiments of van Dijken *et al.*,[8] and is significantly lower than the value obtained if attraction is not taken into account.

C. Dependence on azimuthal angle

While the results presented so far correspond to deposition along the [110] direction (corresponding to an azimuthal angle $\phi = 0°$ with respect to the principal lattice directions, as in the experiments of Ref. 7) for comparison we have also carried out simulations for the case of deposition along the [100] direction corresponding to $\phi = 45°$. As can be seen in Fig. 9, for large deposition angles the azimuthal angle has a significant effect on the surface morphology. In particular, for the case of deposition along the [100] direction and $\theta = 80°$, the ripples are effectively "rotated" so that they remain perpendicular to the beam, but consist of "zigzag" facets oriented along the principal crystal directions. Similarly, for

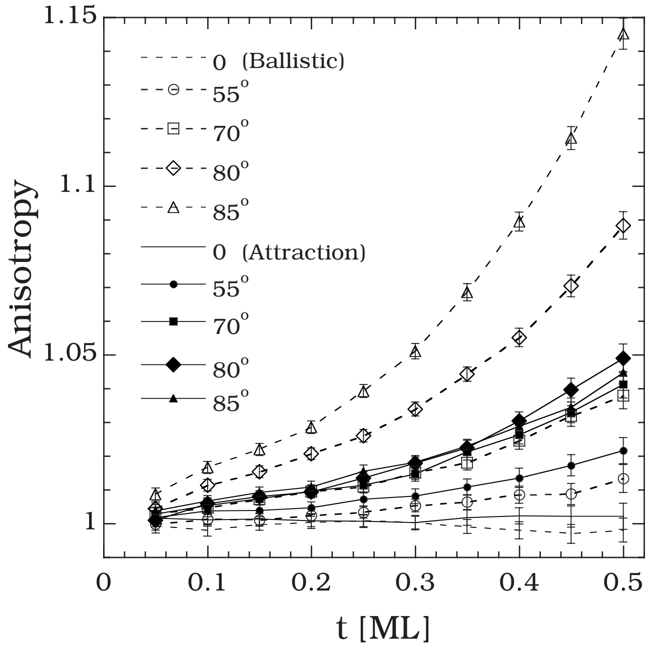

FIG. 8. Same as Fig. 6 but for submonolayer regime.

higher angles (θ=85°), the rod formation observed for deposition along the [110] direction is replaced by the formation of zigzag ripples and rods in the case of deposition along the [100] direction. However, as shown in Fig. 10, despite these dramatic effects on the surface morphology, the surface roughness exhibits only a very weak dependence on the azimuthal angle.

D. Dependence on growth parameters (ballistic deposition)

In previous work[19] it was found that, in general, those factors which enhance mound formation also tend to enhance ripple formation at oblique incidence. In particular, we found that increasing the ES barrier tends to hasten ripple formation, while increasing D/F and/or increasing the rates of edge and/or corner diffusion tends to delay the formation of (111) facets and ripples.[19] Here we present some additional detailed results regarding the dependence of the surface morphology on growth parameters and temperature. Since these simulations are quite time consuming, in most cases they were only carried out for the case of ballistic deposition with restricted search, and in all cases correspond to deposition along the [110] direction (ϕ=0°). However, we expect that the qualitative behavior will be the same in the presence of attraction.

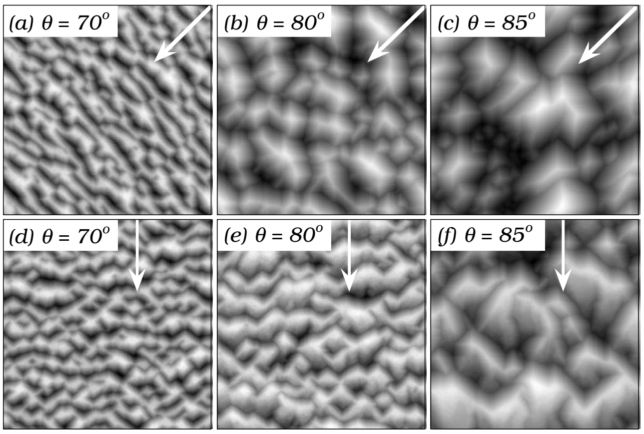

FIG. 9. Comparison of surface morphology obtained for deposition along the [110] direction (top row) with that obtained for deposition along the [100] direction (bottom row) for different deposition angles θ, in the presence of attraction with L=512 at t =50 ML. Arrows indicate deposition direction in each case.

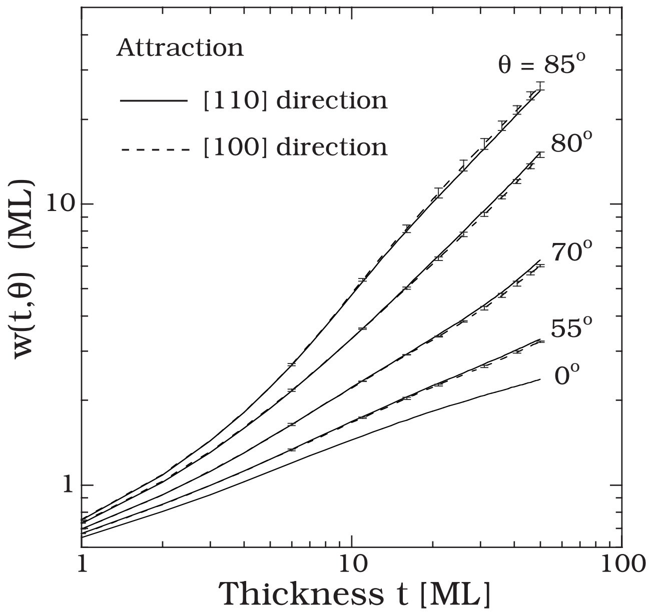

FIG. 10. Surface roughness as function of film thickness for the case of deposition along the [110] direction (solid lines) and along the [100] direction (dashed lines) for different deposition angles θ with $D/F=10^5$ and E_{ES}=0.07 eV.

1. D/F dependence and low-temperature case

In order to understand in more detail the dependence of the surface morphology on deposition parameters, we have carried out simulations with a moderate ES barrier and moderate edge and corner diffusions, but with values of D/F ranging from 5.2×10^3 to 10^7. Figure 11 shows the corresponding results for the perpendicular correlation length $\xi_\perp$ as a function of film thickness for a deposition angle θ =80°. As can be seen in Fig. 11(a), the critical thickness corresponding to the transition to ripple formation increases with increasing D/F, while $\xi_\perp \sim t^n$, where $n \simeq 1/2$ after ripple formation. We note that this value of the ripple coarsening exponent is consistent with a ripple growth mechanism which involves the deposition-induced coalescence of mounds perpendicular to the beam direction and thus corresponds to growth with nonconserved order parameter.

Figure 11(b) shows the corresponding results for the scaled correlation length $\xi_\perp/l_d$ as a function of scaled film thickness t/l_d^2, where $l_d \simeq (D/F)^{1/6}$ is the diffusion length appropriate for our model, for which the critical island size[36,37] is 1 since it corresponds to irreversible growth. As can be

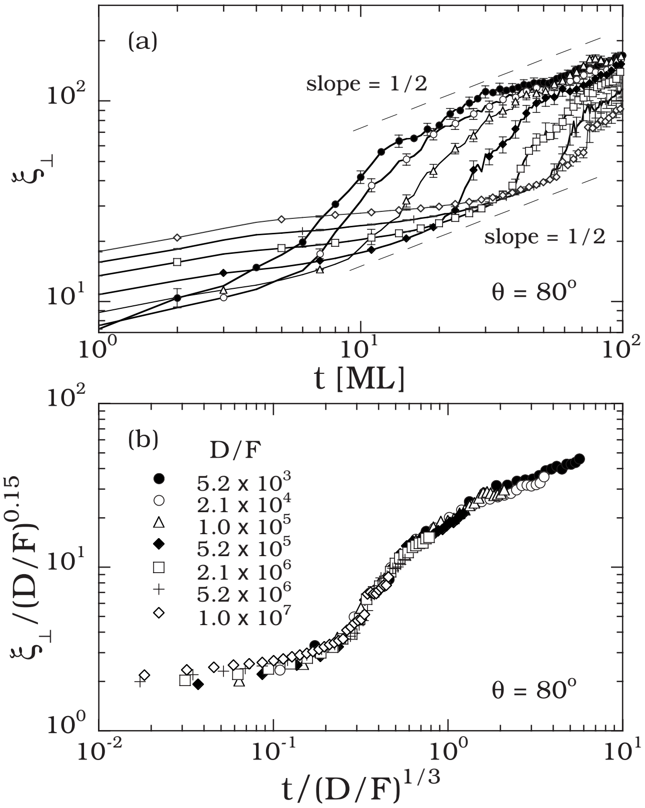

FIG. 11. (a) Correlation length $\xi_\perp$ as a function of film thickness for case of ballistic deposition and $\theta=80°$ with $L=512$ (b) scaled correlation length as a function of scaled film thickness.

seen, there is excellent scaling. In addition, these results indicate that the initial ripple size is determined by the "diffusion length" l_d corresponding to the island and/or mound size in the early stages of growth. They also indicate that the critical thickness t_c for ripple formation scales as $t_c \sim l_d^2$. We have also obtained excellent scaling with the same set of scaling exponents for a deposition angle of 85° (not shown).

In order to further understand the dependence of the surface morphology on D/F as well as the origin of the ripple instability, we have also carried out simulations for the case $D/F=0$, corresponding to a growth temperature which is low enough that both edge diffusion and monomer diffusion on the (100) terrace are suppressed, but still high enough that both DF and fast diffusion on (111) facets remain active. We note that at normal incidence there is no mound instability in this case and the surface is flat and relatively featureless,[21] due to the existence of a downhill surface current which arises from downhill funneling.[25] Figure 12 shows typical pictures of the surface morphology for deposition angles $\theta=70°-88°$ at $t=50$ ML for this case. As can be seen, all the characteristic features and morphological transitions observed previously for the case of moderate D/F ($D/F=10^5$) and ES barrier are also present in this case. These results show clearly that the instability to ripple and/or rod formation is primarily a geometric effect and is not dependent on the existence of an instability to mound formation. We also note that due to the relatively small feature sizes in the early stages of growth, which tend to enhance coalescence and ripple formation, both the ripple and rod transitions occur at smaller thicknesses than for the case of moderate D/F. Figure 13 shows the corresponding scaling results for the relative width deviation as a function of the scaling variable θt^γ, where $\gamma=0.072$. As can be seen, there is excellent scaling over a large range of film thicknesses and depo-

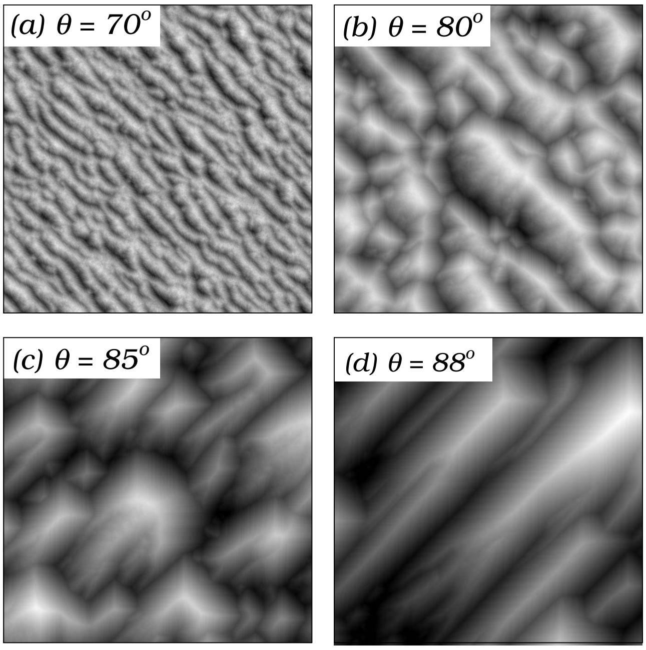

FIG. 12. Gray-scale pictures of surface morphology at $t=50$ ML (512×512 portion of $L=1024$ system) for $\theta=70°-88°$ for the case of ballistic deposition with $D/F=0$.

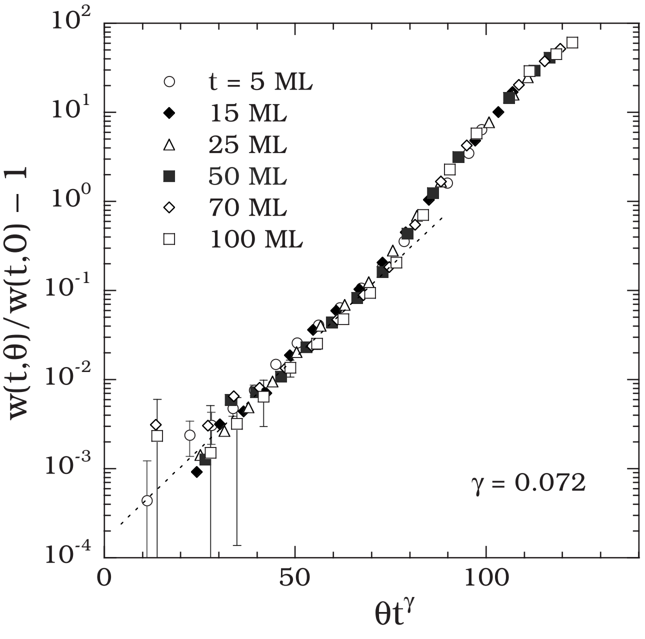

FIG. 13. Relative width deviation $\delta w/w(t,0)$ for the case of ballistic deposition with $D/F=0$ as a function of scaled deposition angle θt^γ for $\theta=10°-88°$ and $t=5-100$ ML. As in Fig. 3(b) the error bars are much smaller than the symbol size for large values of the scaling variable.

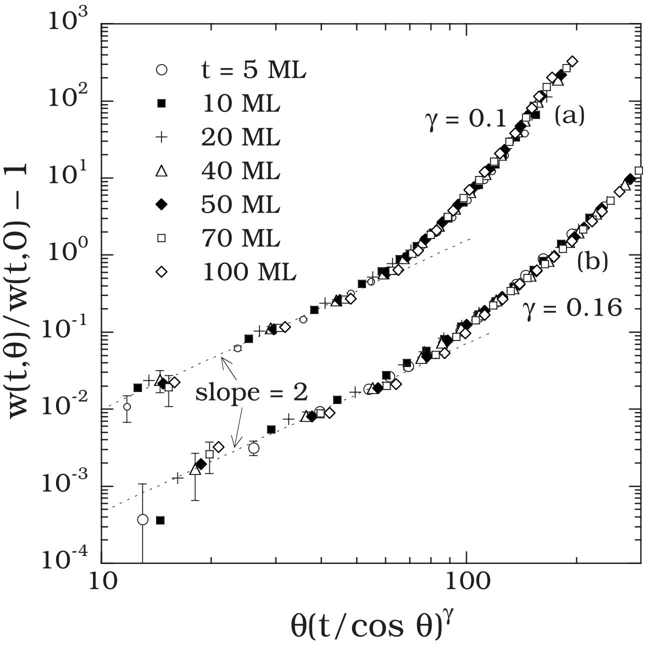

FIG. 14. Relative width deviation $\delta w/w(t,0)$ obtained in ballistic deposition simulations with constant flux as a function of scaled deposition angle for $\theta=10°-88°$ and $t=5-100$ ML. (a) $D/F_0=5000$ and (b) $D/F_0=10^5$. Results for $D/F_0=5000$ have been shifted up by a factor of 10 for clarity.

sition angles. We note that the value of the scaling exponent is very close to that previously obtained in Ref. 19 ($\gamma=0.075$) for the case of ballistic deposition with restricted search and moderate D/F.

2. *Angle-dependent deposition rate* ($F=F_0 \cos\theta$)

In the experiments of van Dijken *et al.*,[7,8] the effusion cell geometry was carefully controlled so as to maintain a constant overall deposition rate F as the deposition angle θ was varied. However, one could easily imagine an experiment in which the deposition flux was kept constant while the deposition angle was varied, thus leading to a deposition-angle dependent deposition rate $F(\theta)=F_0\cos\theta$. In this case, the time taken to complete 1 ML is proportional to $1/\cos\theta$ and as a result, we expect that the scaling variable θt^γ used in the scaling of the relative width deviation should be replaced by a new scaling variable $\theta(t/\cos\theta)^\gamma$. Figure 14 shows the corresponding scaling results, for this case for two different values of D/F_0 (5000 and 10^5). As can be seen, excellent scaling is observed in both cases, although the exponent γ is somewhat higher for $D/F_0=10^5$ than for $D/F_0=5000$. We note that in this case the relative width deviation $\delta w(t,\theta)/w(t,0)$ does not increase exponentially with the scaling variable but roughly as a power law, at least for small values of the scaling variable. This is perhaps not surprising since the increase in D/F with increasing deposition angle leads to smoothing which "opposes" the increase in the roughness due to shadowing. In particular, for both values of D/F_0 one has $\delta w(x)/w \sim x^2$ for $x<80$, where $x=\theta(t/\cos\theta)^\gamma$.

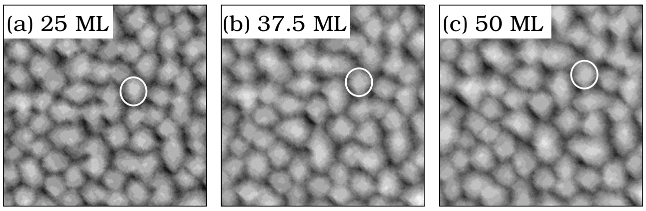
(a) 25 ML
(b) 37.5 ML
(c) 50 ML

FIG. 15. Gray-scale pictures illustrating mound growth and motion toward the beam for the case of ballistic deposition with $\theta=50°$, $D/F=10^5$, and a moderate ES barrier (256×256 portion of $L=512$ system). Circles indicate positions of a given mound at different times.

3. *Dependence of mound speed on deposition angle*

Due to the asymmetry in flux between the illuminated and shadow sides, the asymmetric mounds, ripples, and rods formed in oblique-incidence growth move toward the beam, as can be seen in the pictures in Fig. 15 for different film thicknesses for $\theta=50°$. In order to determine the dependence of the mound speed on deposition angle, we have marked individual mound peaks in our simulations and tracked their motion during the deposition process. We note that in this case ripples are formed at $\theta=80°$.[19] However, some isolated mounds are also observed. By carrying out linear fits to the data, the average mound speed v was measured in units of the nearest-neighbor distance a_1 per ML. As shown in Fig. 16, for small and moderate deposition angles the mound speed increases linearly with deposition angle θ (dashed lines) while for larger angles it increases more rapidly with deposition angle. In particular, for the case of ballistic deposition, we find that the overall dependence of the mound speed on deposition angle is well described by the simple form $v(\theta)\sim\tan(\theta/\sqrt{2})$ up to a deposition angle of $\theta\simeq75°$ at

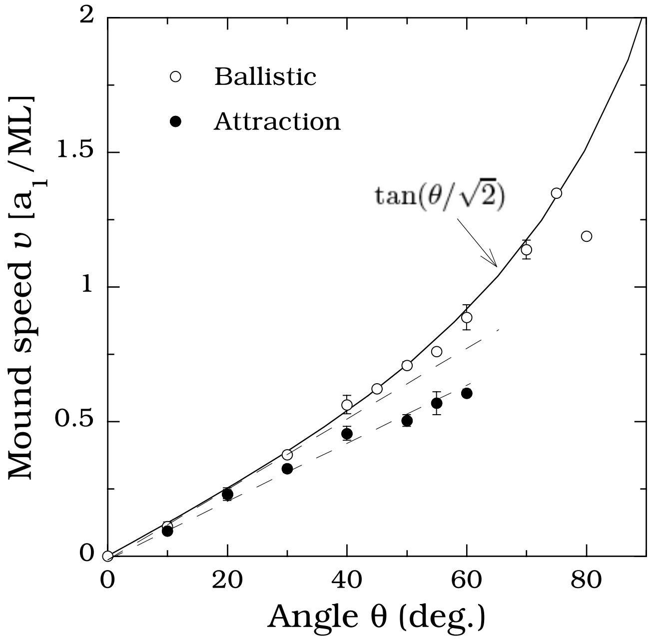

FIG. 16. Mound speed measured in units of the bond distance $a_1=a/\sqrt{2}$ per ML as a function of deposition angle.

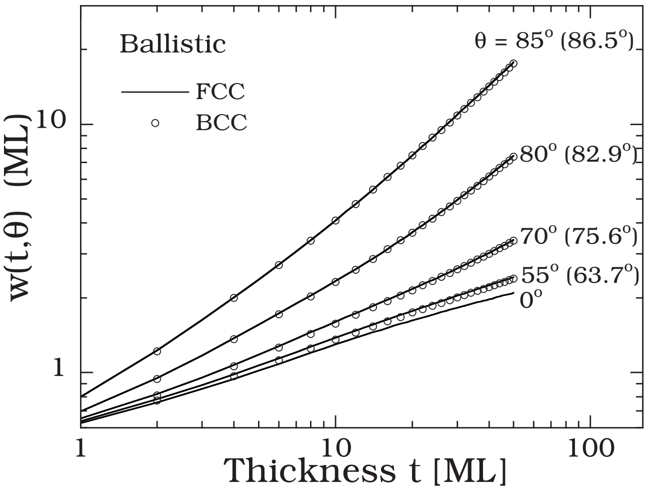

FIG. 17. Comparison of surface roughness obtained in ballistic deposition simulations with $D/F=10^5$ and $E_{\mathrm{ES}}=0.07$ eV with fcc geometry and deposition angle θ and bcc simulations with deposition angle θ_b (in parenthesis) such that $\tan\,\theta_b=\sqrt{2}\,\tan\,\theta$. Error bars (not shown) are smaller than symbol size.

which ripples are formed on the surface. Similar results have also been obtained for the case of deposition with attraction (filled symbols in Fig. 16). However, due to the fact that the "critical" angle for ripple formation is lower in this case, the average mound speed was only measured up to $\theta=60°$. As can be seen, the mound speed is slightly smaller in the case of attraction since the effects of steering due to LR attraction tend to decrease the effective deposition angle [see Fig. 2(b)]. However, it also increases linearly with deposition angle θ up to a deposition angle of 60°.

E. Dependence on crystal geometry

In order to understand the effects of crystal geometry on shadowing we have also carried out ballistic deposition simulations corresponding to slow deposition and moderate ES barrier ($D/F=10^5$ and $E_{\mathrm{ES}}=0.07$ eV) for different deposition angles for the case of a bcc(100) substrate. We note that for a bcc(100) substrate the slope of a step or microfacet is $\sqrt{2}$ times smaller than for a fcc(100) substrate. Therefore, we would expect that if shadowing by microfacets or steps plays the dominant role in determining the surface morphology then, assuming the same set of diffusion barriers and relaxation processes on the surface, the results of oblique-incidence bcc(100) simulations with deposition angle θ_b should be equivalent to growth on a fcc(100) substrate with deposition angle θ if the condition $\tan\,\theta_b=\sqrt{2}\,\tan\,\theta$ is satisfied. Figure 17 shows a comparison between the surface roughness in ML obtained from deposition on an fcc(100) substrate with angle θ and deposition on a bcc(100) substrate with deposition angle θ_b. As can be seen there is excellent agreement between the two results. We note that in the presence of attraction, which becomes particularly important for angles larger than 80°, one might expect that the relationship between θ_b and θ would be slightly modified from the expression above. However, to a good approximation we would expect that even in this case, the results obtained using an fcc(100) model would apply to bcc(100) oblique-incidence growth as long as the relation $\tan\,\theta_b=\sqrt{2}\,\tan\,\theta$ is satisfied. These results also suggest that, in general, ripple and rod formations are likely to occur at somewhat higher deposition angles on bcc(100) substrates than on fcc(100) substrates.

IV. DISCUSSION

We have carried out extensive simulations of a model of oblique-incidence metal (100) growth in order to understand to what extent the effects of steering and flux focusing due to SR and LR attraction, as well as shadowing may affect the surface morphology. For comparison, we have presented the results of simulations both with and without attraction. In both cases, due to computational constraints, we have used a simplified model of deposition, in which a one-atom MD simulation is carried out until the depositing atom is one nearest-neighbor distance away from the nearest film atom, and then "cascades" via DF until it reaches a fourfold hollow site. As already noted, this is a good approximation to the results of a full multiscale MD simulation.

In general, our results indicate that the qualitative picture of oblique-incidence metal (100) growth obtained from earlier ballistic deposition simulations[19] is not fundamentally altered by the inclusion of attraction. In particular, we find that for the case of deposition along the [110] direction there is a series of transitions with increasing deposition angle and film thickness: from asymmetric mounds at moderate deposition angles, to asymmetric ripples oriented perpendicular to the beam at larger deposition angles, and finally to "rods" with (111) facets oriented parallel to the beam at larger deposition angles and/or film thicknesses. However, our results also indicate that the attraction of depositing atoms to the substrate can have several important modifying effects on the surface morphology.

The first effect, due primarily to LR attraction, is a reduction in the anisotropy in the submonolayer regime when compared to ballistic deposition. As indicated by our results for the normalized flux near an island, this is due to the effect of steering which reduces the angle of incidence for large deposition angles and thus tends to reduce the amount of shadowing directly behind submonolayer islands and thus inhibit island coalescence in the beam direction. For very large angles, this effect can also lead to reduced surface roughness in the early stages of multilayer growth.

The second effect is due to flux focusing[7,8] and tends to occur in the multilayer regime. This effect tends to increase the surface roughness and feature size and also reduce the critical thickness for ripple and rod formations. It can also affect the anisotropy in the early stages of multilayer growth. For large deposition angles and film thicknesses this effect also leads to sideways attraction which tends to limit the anisotropy in the rod phase. Our simulation results also indicate that the effects of flux focusing and sideways attraction may explain the experimental observation of symmetric pyramids in Cu/Cu(100) growth for deposition angles and film thicknesses near the transition from ripple to rod formation.

In addition to these results for the surface morphology we have also studied the scaling of the surface roughness as a function of deposition angle and film thickness. In particular, for both ballistic deposition and deposition with attraction, we have found excellent scaling for the relative width deviation compared to normal incidence using the scaling form $\delta w(t,\theta)/w(t,0) \sim f(\theta(t\ /F(\theta)^{\gamma})$ for deposition angles $\theta \geq 55°$. We note that the exponent γ (ranging from $\gamma=0.072$ in the case of restricted search to $\gamma \simeq 0.11$ in the case of extended search both with and without attraction) appears to depend somewhat on the details of the SR interaction but not on the long-range attraction. However, the relatively small value obtained also indicates that the dependence on film thickness t is much weaker than the dependence on deposition angle θ. For the case of a deposition rate which is independent of deposition angle as in the experiments of Ref. 7, the shape of the scaling function indicates that the relative deviation in the surface roughness increases exponentially with deposition angle. The existence of such a scaling form also indicates that while the critical thickness for ripple formation increases rapidly with decreasing deposition angle, for angles which are not too small, a ripple transition will still be observed for sufficiently large thicknesses. It is worth noting that this prediction is in good agreement with recent experimental results.[32]

While we have primarily focused on the case of deposition along the [110] direction, as in the experiments of Ref. 7, we have also carried out simulations corresponding to deposition along the [100] direction in order to examine the dependence on azimuthal angle. This leads to dramatic changes in the surface morphology, including the formation of zigzag ripples perpendicular to the beam at large angles of incidence, as well as a “mixed” rod and ripple phase at larger deposition angles. However, despite these effects on the surface morphology we find that the azimuthal angle has very little effect on the surface roughness.

In order to get a more complete understanding of the dependence of the surface morphology and roughness on deposition parameters, we have also carried out a variety of additional simulations for the case of ballistic deposition and deposition along the [110] direction. In particular, we have studied the scaling of the surface roughness and perpendicular correlation length $\xi_{\perp}$ as functions of film thickness and D/F for fixed deposition angle. Our results indicate that the ripple length increases as $t^{1/2}$ with a prefactor that is approximately proportional to the submonolayer diffusion length or island-spacing $l_d \sim (D/F)^{1/6}$. This result indicates that the initial ripple size is determined by the island and/or mound size in the early stages of growth. Similarly, the “coarsening” exponent of 1/2 is consistent with a ripple growth mechanism which involves the deposition-induced coalescence of mounds perpendicular to the beam direction and thus corresponds to growth with nonconserved order parameter. Our results also indicate that the critical thickness for ripple formation at fixed deposition angle increases as l_d^2 or $(D/F)^{1/3}$. We note, however, that for large deposition angles, the growth perpendicular to the beam is eventually superceded by growth parallel to the beam with $w \sim \xi_{\parallel} \sim t$ leading to rod formation at large film thicknesses.

One particularly interesting case is that of low-temperature growth corresponding to small D/F $(D/F \simeq 0)$, but at temperatures high enough that downward funneling and fast diffusion on (111) facets are still active. While there is no mound instability for this case at normal-incidence deposition, in the case of oblique-angle deposition ripple and rod formations are still observed. This indicates that ripple and rod formations are primarily geometric effects and may occur at low temperature even in the absence of an instability to mound formation. These results also indicate, consistent with our scaling results for the dependence on D/F, that with decreasing temperature the effects of shadowing tend to become important at smaller deposition angles and film thicknesses.

Finally, we note that while the results presented here are based on a generic model of metal (100) oblique-incidence growth, the parameters used in most of our simulations are identical to those previously used[21] to model Fe/Fe(100) growth at normal incidence.[23,24] Accordingly, we expect that with the exception of a slight modification of the deposition angle as described in Sec. III E to account for the bcc geometry, our simulation results may be relevant to the room-temperature oblique-incidence growth of Fe/Fe(100). While these parameters have also been shown[19] to provide good qualitative agreement with oblique-incidence Cu/Cu(100) growth experiments below room temperature,[7,8] it is interesting to consider the possible differences between our model and a model more specific to Cu/Cu(100) growth.[18] One of the main differences is the existence of an extremely low barrier for the diffusion of adatoms along Cu [110] island edges.[33–35,38] The resulting fast edge diffusion enhances the mound instability at normal incidence[5] and also enhances the regularity and ordering of the resulting islands and ripples.[17,18,22]

In summary, we have carried out extensive simulations of a model of oblique-incidence metal (100) growth in order to understand the effects of steering and flux-focusing due to attraction as well as shadowing on the surface morphology. We have also studied the dependence of the surface morphology on a variety of deposition parameters including the azimuthal angle, growth temperature, and flux, as well as deposition angle and film thickness. While our results indicate that much of the qualitative behavior previously observed in experiments[7,8] can be explained by geometric effects which dominate at large deposition angles, we find that the effects of flux focusing and steering due to attraction also play an important role.

ACKNOWLEDGMENTS

This work was supported by NSF Grant No. DMR-0606307 as well as by a grant of computer time from the Ohio Supercomputer Center.

*yshim@physics.utoledo.edu
†vborovi@physics.utoledo.edu
‡jamar@physics.utoledo.edu

[1] *Morphological Organization in Epitaxial Growth and Removal*, edited by Z. Zhang and M. G. Lagally (World Scientific, Singapore, 1998).
[2] J. W. Evans, P. A. Thiel, and M. C. Bartelt, Surf. Sci. Rep. **61**, 1 (2006).
[3] G. Ehrlich and F. G. Hudda, J. Chem. Phys. **44**, 1039 (1966); R. L. Schwoebel, J. Appl. Phys. **40**, 614 (1969).
[4] J. G. Amar, Phys. Rev. B **60**, R11317 (1999).
[5] M. V. Ramana Murty and B. H. Cooper, Phys. Rev. Lett. **83**, 352 (1999); Surf. Sci. **539**, 91 (2003).
[6] O. Pierre-Louis, M. R. D'Orsogna, and T. L. Einstein, Phys. Rev. Lett. **82**, 3661 (1999).
[7] S. van Dijken, L. C. Jorritsma, and B. Poelsema, Phys. Rev. Lett. **82**, 4038 (1999).
[8] S. van Dijken, L. C. Jorritsma, and B. Poelsema, Phys. Rev. B **61**, 14047 (2000).
[9] S. van Dijken, G. Di Santo, and B. Poelsema, Appl. Phys. Lett. **77**, 2030 (2000).
[10] A. M. Mulders A. Fraile Rodríguez, D. Arvanitis, C. Hofer, C. Teichert, M. Á. Niño, J. Camarero, J. J. de Miguel, R. Miranda, K. Lyutovich, E. Kasper, S. Heun, and A. Locatelli, Phys. Rev. B **71**, 214422 (2005).
[11] H.-J. Ernst, F. Fabre, R. Folkerts, and J. Lapujoulade, Phys. Rev. Lett. **72**, 112 (1994).
[12] M. Raible, S. J. Linz, and P. Hanggi, Phys. Rev. E **62**, 1691 (2000).
[13] F. Montalenti and A. F. Voter, Phys. Rev. B **64**, 081401(R) (2001).
[14] J. Yu and J. G. Amar, Phys. Rev. Lett. **89**, 286103 (2002).
[15] J. Seo, S.-M. Kwon, H.-Y. Kim, and J.-S. Kim, Phys. Rev. B **67**, 121402(R) (2003).
[16] J. Seo, H.-Y. Kim, and J.-S. Kim, Phys. Rev. B **71**, 075414 (2005).
[17] J. Seo, H.-Y. Kim, and J.-S. Kim, J. Phys.: Condens. Matter **19**, 486001 (2007).
[18] V. Borovikov, Y. Shim, and J. G. Amar, Phys. Rev. B **76**, 241401(R) (2007).
[19] Y. Shim and J. G. Amar, Phys. Rev. Lett. **98**, 046103 (2007).
[20] For a general discussion of scaling in epitaxial growth, see A. L. Barabasi and H. E. Stanley, *Fractal Concepts in Surface Growth* (Cambridge University Press, Cambridge, 1995).
[21] J. G. Amar and F. Family, Phys. Rev. B **54**, 14742 (1996).
[22] Y. Shim and J. G. Amar, Phys. Rev. B **73**, 035423 (2006).
[23] Y. L. He, H. N. Yang, T. M. Lu, and G. C. Wang, Phys. Rev. Lett. **69**, 3770 (1992).
[24] J. A. Stroscio, D. T. Pierce, M. D. Stiles, A. Zangwill, and L. M. Sander, Phys. Rev. Lett. **75**, 4246 (1995).
[25] J. W. Evans, D. E. Sanders, P. A. Thiel, and A. E. DePristo, Phys. Rev. B **41**, 5410(R) (1990).
[26] A. Bogicevic, S. Ovesson, P. Hyldgaard, B. I. Lundqvist, H. Brune, and D. R. Jennison, Phys. Rev. Lett. **85**, 1910 (2000).
[27] J. Yu and J. G. Amar, Phys. Rev. B **69**, 045426 (2004).
[28] D. E. Sanders and A. E. DePristo, Surf. Sci. **254**, 341 (1991).
[29] A. F. Voter, in *Intermetallic Compounds: Principles and Practice*, edited by J. H. Westbrook and R. L. Fleischer (Wiley, New York, 1995), Vol. 1, p. 77.
[30] J. G. Amar, Phys. Rev. B **67**, 165425 (2003).
[31] Representative error bars are shown in Fig. 3(b) for $t=5,20$, and 50 ML. However, for large values of the scaling variable they are smaller than the symbol size.
[32] H. Wormeester (private communication).
[33] O. Biham, I. Furman, M. Karimi, G. Vidali, R. Kennett, and H. Zeng, Surf. Sci. **400**, 29 (1998).
[34] H. Mehl, O. Biham, I. Furman, and M. Karimi, Phys. Rev. B **60**, 2106 (1999).
[35] I. Furman, O. Biham, J.-K. Zuo, A. K. Swan, and J. F. Wendelken, Phys. Rev. B **62**, R10649 (2000).
[36] J. A. Venables, Philos. Mag. **27**, 697 (1973).
[37] J. A. Venables, G. D. Spiller, and M. Hanbucken, Rep. Prog. Phys. **47**, 399 (1984).
[38] J. Jacobsen (unpublished); T. L. Einstein, J. Jacobsen, and C. Schiff, Bull. Am. Phys. Soc. **42**, 26 (1997).